



HAL
open science

Preparing for InSight: Evaluation of the Blind Test for Martian Seismicity

Martin van Driel, Savas Ceylan, John Francis Clinton, Domenico Giardini,
Hector Alemany, Amir Allam, David Ambrois, Julien Balestra, Bruce
Banerdt, Dirk Becker, et al.

► **To cite this version:**

Martin van Driel, Savas Ceylan, John Francis Clinton, Domenico Giardini, Hector Alemany, et al..
Preparing for InSight: Evaluation of the Blind Test for Martian Seismicity. *Seismological Research
Letters*, 2019, 90 (4), pp.1518-1534. 10.1785/0220180379 . hal-02365912

HAL Id: hal-02365912

<https://hal.science/hal-02365912v1>

Submitted on 17 Jun 2020

HAL is a multi-disciplinary open access archive for the deposit and dissemination of scientific research documents, whether they are published or not. The documents may come from teaching and research institutions in France or abroad, or from public or private research centers.

L'archive ouverte pluridisciplinaire **HAL**, est destinée au dépôt et à la diffusion de documents scientifiques de niveau recherche, publiés ou non, émanant des établissements d'enseignement et de recherche français ou étrangers, des laboratoires publics ou privés.



Open Archive Toulouse Archive Ouverte (OATAO)

OATAO is an open access repository that collects the work of some Toulouse researchers and makes it freely available over the web where possible.

This is an author's version published in: <https://oatao.univ-toulouse.fr/25972>

Official URL : <https://doi.org/10.1785/0220180379>

To cite this version :

van Driel, Martin and Ceylan, Savas and Clinton, John Francis...[et al.] Preparing for InSight: Evaluation of the Blind Test for Martian Seismicity. (2019) Seismological Research Letters, 90 (4). 1518-1534. ISSN 0895-0695

Any correspondence concerning this service should be sent to the repository administrator:

tech-oatao@listes-diff.inp-toulouse.fr

1 Preparing for InSight: Evaluation of the Blind Test for Martian Seismicity

2 Martin van Driel¹, Savas Ceylan¹, John Francis Clinton², Domenico Giardini¹, Hector Alemany¹²,
3 Amir Allam¹⁹, David Ambrois¹², Julien Balestra¹², Bruce Banerdt⁶, Dirk Becker¹³, Maren Böse^{1,2},
4 Marc S. Boxberg¹⁰, Nienke Brinkman¹, Titus Casademont¹³, Jérôme Chèze¹², Ingrid Daubar⁶, Anne
5 Deschamps¹², Fabian Dethof¹³, Manuel Ditz¹⁰, Melanie Drilleau⁵, David Essing¹³, Fabian Euchner²,
6 Benjamin Fernando¹⁸, Raphael Garcia⁷, Thomas Garth¹⁸, Harriet Godwin¹⁸, Matthew P. Golombek⁶,
7 Katharina Grunert¹³, Celine Hadziioannou¹³, Claudia Haindl¹⁸, Conny Hammer², Isabell Hochfeld¹³,
8 Kasra Hosseini¹⁸, Hao Hu¹⁴, Sharon Kedar⁶, Balthasar Kenda⁵, Amir Khan¹, Tabea Kilchling¹³,
9 Brigitte Knapmeyer-Endrun^{16, 17}, Andre Lamert¹⁰, Jiaxuan Li¹⁴, Philippe Lognonné⁵, Sarah
10 Mader^{13, 20}, Lorenz Marten¹³, Franziska Mehrkens¹³, Diego Mercerat⁴, David Mimoun⁷, Thomas
11 Möller¹⁰, Naomi Murdoch⁷, Paul Neumann¹³, Robert Neurath¹³, Marcel Paffrath¹⁰, Mark P. Panning⁶,
12 Fabrice Peix¹², Ludovic Perrin⁸, Lucie Rolland¹², Martin Schimmel¹⁵, Christoph Schröer¹³, Aymeric
13 Spiga⁹, Simon Christian Stähler¹, René Steinmann¹³, Eleonore Stutzmann¹⁵, Alexandre Szenicer¹⁸,
14 Noah Trumpik¹³, Maria Tsekhmistrenko¹⁸, Cédric Twardzik¹², Renee Weber³, Philipp
15 Werdenbach-Jarklowski¹³, Shane Zhang¹¹, and Yingcai Zheng¹⁴

16 ¹Institute of Geophysics, ETH Zürich Sonneggstrasse 5, 8092 Zürich, Switzerland

17 ²Swiss Seismological Service, ETH Zürich Sonneggstrasse 5, 8092 Zürich, Switzerland

18 ³NASA Marshall Space Flight Center, ST13/NSSTC 2047, Huntsville, Alabama 35805 U.S.A.

19 ⁴CEREMA Méditerranée, project team MOUVGS, 500 route des Lucioles, 06903, Sophia Antipolis,
20 France

21 ⁵Institut de Physique du Globe de Paris, Sorbonne Paris Cité, Université Paris Diderot, 75013 Paris,
22 France

23 ⁶Jet Propulsion Laboratory, California Institute of Technology Pasadena, California 91109 U.S.A.

24 ⁷ISAE-SUPAERO, Université de Toulouse, DEOS/ SSPA, 10 av E. Belin, 31400 Toulouse, France

25 ⁸Centre National d'Etudes Spatiales, 18 Avenue Edouard Belin, 31400 Toulouse, France

⁹Laboratoire de Météorologie Dynamique (LMD/IPSL), Sorbonne Université, Centre National de la
Recherche Scientifique, École Polytechnique, École Normale Supérieure, Paris, France

¹⁰Ruhr University Bochum, Faculty of Geosciences, Institute of Geology, Mineralogy and Geophysics,
44780 Bochum, Germany

¹¹Department of Physics, University of Colorado Boulder, Boulder, Colorado 80309, U.S.A.

¹²Université Côte d'Azur, Observatoire de la Côte d'Azur, CNRS, IRD, Géoazur, France

¹³Institute of Geophysics, University of Hamburg, Bundesstrasse 55, 20146 Hamburg, Germany

¹⁴Department of Earth and Atmospheric Sciences, University of Houston, Houston, Texas, U.S.A.

¹⁵Institut de Physique du Globe de Paris, 1 rue Jussieu, 75252 Paris, Cedex 5, France

¹⁶Max-Planck-Institut für Sonnensystemforschung, Justus-von-Liebig-Weg 3, 37077 Göttingen,
Germany

¹⁷now at: Institute of Geology and Mineralogy, University of Cologne, Vinzenz-Pallotti-Str. 26, 51429
Bergisch Gladbach, Germany

¹⁸Department of Earth Sciences, University of Oxford, South Parks Road, Oxford OX1 3AN, UK

¹⁹Department of Geology & Geophysics, University of Utah, Salt Lake City, Utah, U.S.A.

²⁰Karlsruhe Institute of Technology (KIT), Geophysical Institute, Hertzstr. 16, 76187 Karlsruhe,
Germany

April 15, 2019

44 **Abstract**

45 In December 2018, the NASA InSight mission deployed a seismometer on the surface of Mars. In preparation for the
46 data analysis, in July 2017 the Mars Quake Service initiated a blind test, in which participants were asked to detect and
47 characterize seismicity embedded in a one Earth year long synthetic dataset of continuous waveforms. Synthetic data were
48 computed for a single station, mimicking the streams that will be available from InSight as well as the expected tectonic
49 and impact seismicity, and noise conditions on Mars (Clinton et al. 2017). In total, 84 teams from 20 countries registered
50 for the blind test and 11 of them submitted their results in early 2018. The collection of documentations, methods, ideas
51 and codes submitted by the participants exceeds 100 pages. The teams proposed well established as well as novel methods
52 to tackle the challenging target of building a global seismicity catalogue using a single station. This paper summarizes
53 the performance of the teams, and highlights the most successful contributions.

54 **Introduction**

55 The National Aeronautics and Space Administration (NASA) discovery-class mission InSight (Interior exploration using
56 Seismic Investigations, Geodesy and Heat Transport, Banerdt et al. 2013, <http://insight.jpl.nasa.gov>) to Mars was
57 launched on May 5th, 2018 and landed successfully on November 26th. It is dedicated to determining the constitution
58 and interior structure of Mars. For this purpose, InSight deployed a single seismic station with both broadband and
59 short-period seismometers on the surface of Mars, together with a number of other geophysical (Folkner et al. 2018; Spohn
60 et al. 2018) and meteorological (Spiga et al. 2018) sensors. The seismic instrument package (SEIS) is specifically designed
61 for martian conditions to record marsquakes as well as meteoroid impacts, and transmit data back to Earth for analysis
62 (Lognonné et al. 2019, www.seis-insight.eu).

63 The Marsquake Service (MQS, Clinton et al. 2018) is tasked with the prompt review, detection and location of all
64 martian seismicity recorded by InSight. It will also manage the seismicity catalogue, refining locations using the best
65 available Mars models as they are developed during the project. To prepare the InSight science team and the wider
66 seismological community for the data return, the MQS sent an open invitation to participate in a blind test to detect and
67 locate seismic events hidden in a synthetic data set, which was published in SRL in July 2017 (Clinton et al. 2017). The
68 data set was made available at <http://blindtest.mars.ethz.ch/> in August 2017 with mandatory registration. Following
69 the submission deadline in February 2018, the true model and event catalogue together with the original waveform data
70 are now openly available online.

71 **Purpose of the Test**

72 The blind test was initiated with the main purpose of improving and extending the set of methods for event location,
73 discrimination and magnitude estimation as well as phase identification and source inversion to be applied in routine

74 analysis of the InSight data set by collecting ideas from outside the InSight science team. It also helped to raise the profile
75 of the InSight mission and to familiarize interested scientists with the data set to be expected from Mars.

76 Beyond this, the test also initiated a major effort to generate a single, consistent, temporal, synthetic data set that
77 collected all best pre-landing estimates of seismicity, impacts, synthetic seismograms, atmospheric pressure variations and
78 related noise, instrument self-noise and 1D structure models. The data set was made available in the same formats, and
79 using similar web services as are now available for the real data from Mars. For this reason, the data set was also used
80 for various operational readiness tests as well as scientific testing purposes in preparation for data return.

81 Furthermore, the submitted catalogues allow to derive detection and location thresholds as a function of magnitude and
82 distance, that are not based on simple signal to noise ratio assumptions, but include the whole complexity of identifying
83 and locating events in the time series. It is important to note though, that this data set included randomly distributed
84 events over the sphere. Compared to the global fault distribution (Knapmeyer et al. 2006), this model may have too
85 many events near the landing site, so the total number of detectable events in this dataset may be higher than predicted
86 by recent seismicity models of similar total activity (Plesa et al. 2018). This needs to be accounted for if the detection
87 threshold determined in this test is used for constraining seismic activity rates.

88 In the invitation, we envisioned a quantitative scoring in different categories (event detection and localization accuracy
89 in different magnitude classes, impact discrimination and focal mechanism), but this turned not to be feasible given the
90 heterogeneity of the submissions and relatively small number of detectable events in the data. Instead, we decided to
91 focus on visual comparisons of the performances and compare them to the level 1 (L1) requirements of the mission, i.e.
92 the required accuracy to achieve InSight’s science objectives. The L1 requirements for quake location are 25% in distance
93 and 20 degrees in azimuth (Banerdt et al. 2013).

94 **Overview of the Test Data Set**

95 The event catalogue included a total of 204 tectonic marsquakes as well as 36 impacts (Fig. 1), with only a fraction of
96 them producing seismic signals above the noise level. The events were randomly distributed over the whole planet where
97 the depth distribution of tectonic events followed a skewed Gaussian distribution with a maximum allowed depth of 80
98 km. The maximum event size was $M_w = 5$ and the magnitude-frequency distribution approximates a Gutenberg-Richter
99 distribution with $a = 4.88$, $b = 1$; events with $M_w < 2.5$ were neglected (see Fig. 2 and Ceylan et al. 2017).

100 The impact catalogue is based on Teanby (2015) and the size distribution of observed newly dated craters (Daubar
101 et al. 2018), again assuming a globally random distribution. To restrict amplitudes to levels similar to $M_w 2.5$ events, we
102 only include impacts with impactor mass larger than 100 kg and assume an impact velocity of 10 km/s.

103 The seismic signals were computed using AxiSEM (Nissen-Meyer et al. 2014) and Instaseis (van Driel et al. 2015) as
104 solutions to the elastic-wave equation in radially symmetric planet models. Continuous time series were then created by

105 superimposing the event based data with seismic noise that reflects the pre-landing estimates for the surface installed
106 instruments at the landing site (Murdoch et al. 2017a; Murdoch et al. 2017b; Mimoun et al. 2017; Kenda et al. 2017). It
107 includes noise generated by the sensors and systems themselves, as well as through sources in martian environment (such
108 as fluctuating pressure-induced ground deformation, the magnetic field, and temperature-related noise) and nearby lander
109 (such as wind-induced solar panel vibrations).

110 Synthetic data were generated from one of the 14 candidate models (Zharkov and Gudkova 2005; Rivoldini et al. 2011;
111 Khan et al. 2016) which were published as part of the data set, but the model choice was not revealed to participants.
112 The model used for creation of waveform data set is shown in Figure 3 which explains two prominent features observed
113 by most participating teams: 1) Clear S-wave arrivals were absent in most events due to the low velocity region in the
114 upper mantle, which made distance estimations based only on relative P and S travel times very difficult, and 2) at the
115 same time, the bedrock layer at the surface acted as a wave guide and caused a prominent P-coda arrival, that could be
116 used for estimating locations in this 1D setting (see Fig. 4 for an overview of the most visible events). Such a phase is
117 observed over long distances in specific settings on Earth, such as oceanic crust of constant thickness (e.g. Kennett and
118 Furumura 2013), but in this blind test, it should be considered an artifact from the simple 1D model. It is not expected
119 to be observed as a global phenomenon on Mars due to attenuation from 3D scattering.

120 An overview of responsibilities for the generation of the data set can be found in Table 1; further details can be found
121 in Clinton et al. (2017). Based on the experience gained and performance of the MQS in particular within this test, the
122 MQS is currently refining the location strategies and running an ORT (operational readiness test) with synthetic data
123 computed in a 3D model.

124 In the following sections, we first summarize the methods used by each team. Then, we compare the success of each
125 submission in terms of event detection, as well as estimated event distance, back-azimuth and origin time against the true
126 event parameters.

127 **Participation and Methods**

128 In order to ensure effective communication with participants or anyone who wanted to experiment, registration for the
129 test was mandatory for accessing the dataset. On the other hand, participation was completely voluntary; but we strongly
130 encouraged all registrants to submit their results, particularly with event catalogues. In total, 84 teams registered and 11
131 of them submitted their analysis. Due to the lack of feedback, we do not have a further overview on how test data was
132 used by other teams that downloaded the data but chose not to participate.

133 The participating teams were composed of researchers both from inside (IPGP, MQS, Max Planck) and outside (Col-
134 orado, Geoazur, Houston, Utah) the InSight science team. Participant profiles were rather diverse including senior
135 researchers as well as PhD (Bochum, Oxford), masters (Hamburg) and even high school students (SEISonMars@school).

136 See Table 2 for a list of the teams and their members. In Table 3, we summarize the wealth of methods used by the
137 participants with references to previous publications as much as possible, but a significant fraction of the methods applied
138 by participants appears to have been developed specifically for this test.

139 Most teams inspected the waveforms visually or used spectrograms for event detection, while four teams (Bochum,
140 Geoazur, Hamburg, Utah) also utilized STA/LTA algorithms with manual review for this purpose. In the case of a
141 single station, event distance can be estimated using relative travel times between different body- and surface waves,
142 and multi-orbit surface waves for the larger events. While the latter is independent of the model (Panning et al. 2017),
143 body and minor arc surface wave travel times need a reference model for distance estimation. Hence, most teams tried
144 to first determine the model from the 14 candidate models and then computed locations for that model. Three teams
145 (Bochum, Colorado, MQS), however, used probabilistic methods to account for the inherent trade off between model
146 and distance. Combining the distance estimate with the back-azimuths of the event and the known station location,
147 an absolute location can be derived. The participants used a large variety of both P and Rayleigh polarization analysis
148 methods for this purpose. Only two teams (Houston and MQS) attempted to determine depth, which was difficult as most
149 events did not show clear depth-phases.

150 Only one team (Colorado) attempted to decorrelate the atmospheric pressure signals to reduce the noise; and one other
151 team (Hamburg) classified pressure events automatically, while others relied on a visual check to exclude those from the
152 catalogue. The Houston team was the only group to derive surface wave phase velocities. Two teams did not submit a
153 catalogue but applied methods that facilitate event detection and phase recognition: IPGP focused on crustal structure
154 and polarization analysis rather than event locations and Max Planck implemented an HMM (Hidden Markov Models)
155 approach to detect events, which allowed them to provide only event detection times and no origin times.

156 None of the teams submitted information on the focal mechanisms within this test, but the method of Stähler and
157 Sigloch (2014) has been applied successfully after the submission deadline by the MQS team for the largest 3 events
158 (Clinton et al. 2018).

159 Performance

160 In the blind test announcement (Clinton et al. 2017), it was stated that it was mandatory to provide a location and
161 origin time. A number of teams were only able to provide approximate detection times without locations and others only
162 provided locations for parts of their catalogue. We decided to also show these results, though we understand that other
163 teams that closely followed this rule may have left out detected events that they were not able to locate and hence the
164 detection statistics needs to be interpreted with care.

165 Figure 5 gives an overview of the performance by different teams in detecting and locating events:

- 166 • The blue bars represent the total number of events in each catalogue, that besides true and false detections, may also

167 include multiple detections for a single event. This was in particular the case for the fully automatic Hidden Markov
168 Model (HMM) approach from the Max Planck team, since HMM is fundamentally a pattern matching approach
169 operating on certain statistics that heavily relies on proper classification and representation of training events. In
170 this application, only a single training event was used.

- 171 • The orange bars represent the number of events that could be associated with an event in the true catalogue solely
172 based on the origin time and with duplicate detections removed. As we prevented event waveforms from overlapping
173 in the seismicity catalogue, the association is straightforward. We assume any event time submitted that occurs
174 within a window from 750 seconds before and 1500 seconds after the true origin time as correct. The three teams
175 that performed best in detection (MQS, Hamburg, Bochum) all relied on a high degree of visual data inspection,
176 while two of them (Hamburg, Bochum) assisted by STA/LTA triggering. Comparing seismic and pressure data
177 visually allowed these teams to exclude most non-seismic events. MQS produced daily spectrograms that were
178 visually scanned by different members of the team, which proved a very effective way to maximize event detection.
- 179 • The green bars represent the number of events for which full location information was provided (origin time, distance
180 and azimuth).
- 181 • Finally, the red bars represents events that were located within the InSight mission L1 requirements for location
182 accuracy.

183 Figure 6 shows a more detailed view of the 10 submitted catalogues, highlighting false detections (blue vertical lines) as
184 well as detection and location of quakes (circles) impacts (star symbols). The rate of correct detection and location as well
185 as false detections varies significantly over the time span of the dataset. This may be related to sharing of the workload
186 between multiple operators; for example MQS split the initial detection on a monthly bases between team members.

187 In the following, we focus on the six teams that provided the most complete results in terms of the number of events
188 correctly located within L1 requirements: Bochum, Geoazur, Hamburg, Houston, MQS and Oxford. MQS submitted two
189 catalogues (focusing on absolute and relative distances, respectively), but as they are of very similar quality and were
190 built iteratively using information from both approaches, we treat them as one for the purpose of this paper.

191 **Distance Magnitude Trade-off**

192 Figure 7 provides an overview of the six most complete catalogues with respect to distance and magnitude. It also reveals
193 that although MQS had the highest number of correct detections, a handful of events were missed that other teams were
194 able to detect, and some detected events were located more precisely by other teams. MQS carefully analyzed each of
195 these events again to identify the root cause of these mislocations and unidentified events. Besides mislabeled seismic
196 phases, several issues in the MQS workflow were recognized and resolved, with the most important improvement being
197 the increase of the overlap in the daily plots used for visual screening.

198 Most of the six teams detected all events above magnitude 4, globally. Between magnitude 3 and 4, several teams
199 detected all events until approximately 40 degree distance, even though they could not locate them within the L1 require-
200 ments. MQS detected all events above magnitude 3.5 and all events above magnitude 2.5 within 30 degree distance, which
201 suggests that the detection threshold may be even lower than 2.5 for regional events. The detection curve for MQS is only
202 distance/magnitude dependent, without an indication of an effect of different focal mechanisms.

203 **Distance Estimation**

204 Distance estimation (Fig. 8) was complicated by the low velocity layers in the upper mantle, which made S-waves very
205 hard to identify in the data with the given noise. An easy estimate based only on the traveltimes difference between P and
206 S phase could hence not be applied to most events. On the other hand, Rayleigh wave group arrival times could be used
207 with unrealistically high accuracy in this 1D model, which is one reason for running the current ORT with 3D synthetics.
208 This new test suggests that including estimates of crustal thickness variations from gravity (Wieczorek and Zuber 2004),
209 topography from MOLA (Mars Orbiting Laser Altimeter), and ellipticity lateral variations of surface wave arrival times
210 of up to a few hundred seconds should be expected.

211 An additional simplification was employed by most teams by determining the correct model from the 14 candidate
212 models based on the biggest event in the dataset (see table 3) and then using that model to locate the smaller events. In
213 practice, a number of small events are expected to be seen in the data before any event that is big enough to constrain
214 the model. To add this complexity to the problem, the data in the new 3D test was released in weekly chunks.

215 The MQS catalogue included a data quality classification, where reliable locations were classified as quality A,
216 unreliable locations as quality B, and very unreliable/unconstrained locations as quality C. This figure indicates that only
217 class C and a few class B events could not be located correctly (Clinton et al. 2018).

218 **Back-Azimuth Estimation**

219 The back-azimuth estimation in Figure 9 reveals that some methods suffer from a 180° ambiguity, which can however
220 be resolved by either assuming retrograde Rayleigh motion or including the incidence angle in P-wave azimuth estimates
221 (Panning et al. 2015; Böse et al. 2016). Like for the distance estimate, all MQS quality A and the majority of quality B
222 location estimates meet the L1 requirement.

223 **Origin Time Estimation**

224 The error in origin time estimation is closely related to distance estimation by the fixed model set that was provided for
225 this test, and this can also be observed in the strong correlation in performance for distance and origin time (Fig. 10).
226 Similar arguments as in the distance estimation apply for the model complexities and 3D effects.

Impact Discrimination

Only one team (MQS) classified the event type as quake/impact in their catalogue. Only a single event was identified as an impact, which was correct, and no other event was mis-labeled as impact. MQS did miss the biggest impact event of the dataset in the detection stage. Hence we cannot evaluate the distinction capability in this test and just document the three strongest impact events together with three quakes for reference in Figure 11: If the signal is above the noise, the waveforms appear very distinct from quakes due to trapped energy in the high Q shallow layers of the 1D model as well as very short period surface waves excited by the surface source. In contrast, quakes at depth neither excite trapped waves in the shallow layers in this 1D model due to Snel's law nor the very short period surface waves due to their limited penetration depth.

MQS' classification of the impact was purely based on the waveform's appearance, which they recognised as very different from all other events. With very few impact events ever seismically recorded and the distinct impact behaviour due to the atmosphere on Earth compared to the Moon, there is no well established discrimination technique. Gudkova et al. (2011) suggest a different spectral content of impacts compared to quakes for the Moon. Other criteria include the depth of the event, although the absence of depth phases is difficult to demonstrate. Additionally, newly detected craters on satellite images from Mars might help to discriminate impact events if they can be correlated in time and location.

Conclusions

The submissions to this blind-test have provided the InSight science team with a range of new ideas and brought the specific challenges of single station seismology on Mars to a broader range of seismologists from the general community. In practice, the main benefits of the test to the MQS was that it provided the opportunity to thoroughly test software and routines as well as benchmark the event detection and location capabilities on a previously unavailable quality data set; and to evaluate whether there are new or existing methodologies that were overlooked and could significantly improve MQS' performance.

Finally, various teams contributed to this 1D test with a number of useful and different ideas; however, the algorithms established in MQS produced comparable or better performance. Further evaluation in the light of the 3D effects from synthetics as well as the actual seismicity observed by the InSight seismometers will be necessary to decide if MQS will adopt any of the suggested methods from other teams. From the test it is also obvious that the best performances were produced by the teams that had the time to dedicate to the test – an important lesson for MQS for organizing routine operations: one team member is always on duty to analyze all new data for possible seismic events with another person as backup. Any suspected event is then analyzed carefully by the review team before communicating to the whole science team (see Clinton et al. 2018, for details on the operations).

The blind test experience has helped forming the basis for the currently running operational readiness tests with 3D

258 synthetic data for both the MQS and MSS (Mars Structure Service Panning et al. 2017), which give an opportunity to
259 the operational teams to train daily data review.

260 Data and Resources

261 The test data set is described in more detail by Clinton et al. (2017) and available online at [http://blindtest.mars.
262 ethz.ch/](http://blindtest.mars.ethz.ch/) (last accessed December 2018). Figures are created using ObsPy (Krischer et al. 2015). Submissions (catalogues
263 and documentation) by individual teams are not publicly available.

264 Acknowledgements

265 The co-author list of this paper includes contributors to the evaluation (up to and including D. Giardini), contributors to
266 the data set and invitation paper (Table 1) as well as the participants of the blind test (Table 2).

267 This work was jointly funded by (1) Swiss National Science Foundation and French Agence Nationale de la Recherche
268 (SNF-ANR project 157133 “Seismology on Mars”), (2) Swiss State Secretariat for Education, Research and Innovation
269 (project “MarsQuake Service—Preparatory Phase”) and (3) ETH Zurich (project “Preparatory phase for Mars InSight
270 Ground Segment Support”). Additional support came from the Swiss National Supercomputing Centre (CSCS) under
271 project ID s682. Some of the research described in this article was supported by the InSight (Interior exploration using
272 Seismic Investigations, Geodesy and Heat Transport) project, Jet Propulsion Laboratory, California Institute of Technol-
273 ogy, under a contract with the National Aeronautics and Space Administration (NASA). The Houston team was partially
274 funded by EAR-1621878. A. Spiga and L. Rolland acknowledge funding by CNES (Centre National d’Études Spatiales).
275 This paper constitutes InSight Contribution Number 93.

276 References

- 277 Allam, A. A., Y. Ben-Zion, and Z. Peng (2014). Seismic Imaging of a Bimaterial Interface Along the Hayward Fault, CA,
278 with Fault Zone Head Waves and Direct P Arrivals, *Pure Appl. Geophys.* **171.11** 2993–3011.
- 279 Allam, A. A., V. Schulte-Pelkum, Y. Ben-Zion, C. Tape, N. Ruppert, and Z. E. Ross (2017). Ten kilometer vertical Moho
280 offset and shallow velocity contrast along the Denali fault zone from double-difference tomography, receiver functions,
281 and fault zone head waves, *Tectonophysics* **721** 56–69.
- 282 Banerdt, W. B., S. Smrekar, P. Lognonné, T. Spohn, S. Asmar, D. Banfield, L. Boschi, U. Christensen, V. Dehant, W. M.
283 Folkner, D. Giardini, W. Goetze, M. P. Golombek, M. Grott, T. Hudson, C. Johnson, G. Kargl, N. Kobayashi, J. Maki,
284 D. Mimoun, A. Mocquet, P. Morgan, M. P. Panning, W. Pike, J. Tromp, T. van Zoest, R. Weber, M. A. Wieczorek,

285 R. F. Garcia, and K. Hurst (2013). InSight: A Discovery Mission to Explore the Interior of Mars, *44th Lunar Planet.*
286 *Sci. Conf.* 1915.

287 Bayer, B., R. Kind, M. Hoffmann, X. Yuan, and T. Meier (2012). Tracking unilateral earthquake rupture by P-wave
288 polarization analysis, *Geophys. J. Int.* **188.3** 1141–1153.

289 Böse, M., J. F. Clinton, S. Ceylan, F. Euchner, M. van Driel, A. Khan, D. Giardini, P. Lognonné, and W. B. Banerdt
290 (2016). A Probabilistic Framework for Single-Station Location of Seismicity on Earth and Mars, *Phys. Earth Planet.*
291 *Inter.* **262** 48–65.

292 Böse, M., D. Giardini, S. Stähler, S. Ceylan, J. F. Clinton, M. van Driel, A. Khan, F. Euchner, P. Lognonné, and W. B.
293 Banerdt (2018). Magnitude Scales for Marsquakes, *Bull. Seismol. Soc. Am.* **108.5A** 2764–2777.

294 Ceylan, S., M. van Driel, F. Euchner, A. Khan, J. F. Clinton, L. Krischer, M. Böse, S. C. Stähler, and D. Giardini (2017).
295 From Initial Models of Seismicity, Structure and Noise to Synthetic Seismograms for Mars, *Space Sci. Rev.* **211.1-4**
296 595–610.

297 Clinton, J., D. Giardini, M. Böse, S. Ceylan, M. van Driel, F. Euchner, R. F. Garcia, S. Kedar, A. Khan, S. C. Stähler, B.
298 Banerdt, P. Lognonne, E. Beucler, I. Daubar, M. Drilleau, M. Golombek, T. Kawamura, M. Knapmeyer, B. Knapmeyer-
299 Endrun, D. Mimoun, A. Mocquet, M. Panning, C. Perrin, and N. A. Teanby (2018). The Marsquake Service: Securing
300 Daily Analysis of SEIS Data and Building the Martian Seismicity Catalogue for InSight, *Space Sci. Rev.* **214.8**.

301 Clinton, J., D. Giardini, P. Lognonné, B. W. Banerdt, M. van Driel, M. Drilleau, N. Murdoch, M. P. Panning, R. Garcia,
302 D. Mimoun, M. Golombek, J. Tromp, R. Weber, M. Böse, S. Ceylan, I. Daubar, B. Kenda, A. Khan, L. Perrin, and
303 A. Spiga (2017). Preparing for InSight: An Invitation to Participate in a Blind Test for Martian Seismicity, *Seismol.*
304 *Res. Lett.* **88.5** 1290–1302.

305 Daubar, I., P. Lognonné, N. A. Teanby, K. Miljkovic, J. Stevanović, J. Vaubaillon, B. Kenda, T. Kawamura, J. Clinton, A.
306 Lucas, M. Drilleau, C. Yana, G. S. Collins, D. Banfield, M. Golombek, S. Kedar, N. Schmerr, R. Garcia, S. Rodriguez,
307 T. Gudkova, S. May, M. Banks, J. Maki, E. Sansom, F. Karakostas, M. Panning, N. Fuji, J. Wookey, M. van Driel,
308 M. Lemmon, V. Ansan, M. Böse, S. Stähler, H. Kanamori, J. Richardson, S. Smrekar, and W. B. Banerdt (2018).
309 Impact-Seismic Investigations of the InSight Mission, *Space Sci. Rev.* **214.8**.

310 Eisermann, A. S., A. Ziv, and G. H. Wust-Bloch (2015). Real-Time Back Azimuth for Earthquake Early Warning, *Bull.*
311 *Seismol. Soc. Am.* **105.4** 2274–2285.

312 Fernando, B., M. Tsekhmistrenko, and K. Hosseini (2018). Training martian seismologists for InSight, *Astron. Geophys.*
313 **59.5** 5.17–5.21.

314 Folkner, W. M., V. Dehant, S. Le Maistre, M. Yseboodt, A. Rivoldini, T. Van Hoolst, S. W. Asmar, and M. P. Golombek
315 (2018). The Rotation and Interior Structure Experiment on the InSight Mission to Mars, *Space Sci. Rev.* **214.5**.

316 Gudkova, T. V., P. Lognonné, and J. Gagnepain-Beyneix (2011). Large impacts detected by the Apollo seismometers:
317 Impactor mass and source cutoff frequency estimations, *Icarus* **211.2** 1049–1065.

318 Hammer, C., M. Ohrnberger, and D. Fäh (2013). Classifying seismic waveforms from scratch: A case study in the alpine
319 environment, *Geophys. J. Int.* **192.1** 425–439.

320 Hammer, C., M. Beyreuther, and M. Ohrnberger (2012). A seismic-event spotting system for volcano fast-response systems,
321 *Bull. Seismol. Soc. Am.* **102.3** 948–960.

322 Jurkevics, A. (1988). Polarization analysis of three-component array data, *Bull. Seism. Soc. Am* **78.5** 1725–1743.

323 Kenda, B., P. Lognonné, A. Spiga, T. Kawamura, S. Kedar, W. B. Banerdt, R. Lorenz, D. Banfield, and M. Golombek
324 (2017). Modeling of Ground Deformation and Shallow Surface Waves Generated by Martian Dust Devils and Perspec-
325 tives for Near-Surface Structure Inversion, *Space Sci. Rev.* **211.1-4** 501–524.

326 Kennett, B. L. and T. Furumura (2013). High-frequency Po/So guided waves in the oceanic lithosphere: I-long-distance
327 propagation, *Geophys. J. Int.* **195.3** 1862–1877.

328 Khan, A., M. van Driel, M. Böse, D. Giardini, S. Ceylan, J. Yan, J. F. Clinton, F. Euchner, P. Lognonné, N. Murdoch, D.
329 Mimoun, M. Panning, M. Knapmeyer, and W. B. Banerdt (2016). Single-station and single-event marsquake location
330 and inversion for structure using synthetic Martian waveforms, *Phys. Earth Planet. Inter.* **258** 28–42.

331 Knapmeyer, M., J. Oberst, E. Hauber, M. Wählisch, C. Deuchler, and R. Wagner (2006). Working models for spatial
332 distribution and level of Mars’ seismicity, *J. Geophys. Res.* **111.E11** E11006.

333 Knapmeyer-Endrun, B. and C. Hammer (2015). Identification of new events in Apollo 16 lunar seismic data by Hidden
334 Markov Model-based event detection and classification, *J. Geophys. Res. Planets* **120.10** 1620–1645.

335 Krischer, L., T. Megies, R. Barsch, M. Beyreuther, T. Lecocq, C. Caudron, and J. Wassermann (2015). ObsPy: a bridge
336 for seismology into the scientific Python ecosystem, *Comput. Sci. Discov.* **8.1** 014003.

337 Lin, F. C., V. C. Tsai, and B. Schmandt (2014). 3-D crustal structure of the western United States: Application of
338 Rayleigh-wave ellipticity extracted from noise cross-correlations, *Geophys. J. Int.* **198.2** 656–670.

339 Lognonné, P. et al. (2019). SEIS: Insight’s Seismic Experiment for Internal Structure of Mars, *Space Sci. Rev.* **215.1**.

340 Mimoun, D., N. Murdoch, P. Lognonné, K. Hurst, W. T. Pike, J. Hurley, T. Nébut, and W. B. Banerdt (2017). The Noise
341 Model of the SEIS Seismometer of the InSight Mission to Mars, *Space Sci. Rev.* **211.1-4** 383–428.

342 Murdoch, N., B. Kenda, T. Kawamura, A. Spiga, P. Lognonné, D. Mimoun, and W. B. Banerdt (2017a). Estimations
343 of the Seismic Pressure Noise on Mars Determined from Large Eddy Simulations and Demonstration of Pressure
344 Decorrelation Techniques for the Insight Mission, *Space Sci. Rev.* **211.1-4** 457–483.

345 Murdoch, N., D. Mimoun, R. F. Garcia, W. Rapin, T. Kawamura, P. Lognonné, D. Banfield, and W. B. Banerdt (2017b).
346 Evaluating the Wind-Induced Mechanical Noise on the InSight Seismometers, *Space Sci. Rev.* **211.1-4** 429–455.

- 347 Nissen-Meyer, T., M. van Driel, S. C. Stähler, K. Hosseini, S. Hempel, L. Auer, A. Colombi, and A. Fournier (2014).
348 AxiSEM: broadband 3-D seismic wavefields in axisymmetric media, *Solid Earth* **5.1** 425–445.
- 349 Panning, M., É. Beucler, M. Drilleau, A. Mocquet, P. Lognonné, and W. B. Banerdt (2015). Verifying single-station seismic
350 approaches using Earth-based data: Preparation for data return from the InSight mission to Mars, *Icarus* **248** 230–242.
- 351 Panning, M., P. Lognonné, W. Bruce Banerdt, R. Garcia, M. Golombek, S. Kedar, B. Knapmeyer-Endrun, A. Mocquet,
352 N. A. Teanby, J. Tromp, R. Weber, É. Beucler, J.-F. Blanchette-Guertin, E. Bozdağ, M. Drilleau, T. Gudkova, S.
353 Hempel, A. Khan, V. Lekić, N. Murdoch, A.-C. Plesa, A. Rivoldini, N. Schmerr, Y. Ruan, O. Verhoeven, C. Gao,
354 U. Christensen, J. F. Clinton, V. Dehant, D. Giardini, D. Mimoun, W. Thomas Pike, S. Smrekar, M. Wiczorek, M.
355 Knapmeyer, and J. Wookey (2017). Planned Products of the Mars Structure Service for the InSight Mission to Mars,
356 *Space Sci. Rev.* **211.1-4** 611–650.
- 357 Plesa, A. C., M. Knapmeyer, M. Golombek, D. Breuer, M. Grott, T. Kawamura, P. Lognonné, N. Tosi, and R. C. Weber
358 (2018). Present-Day Mars’ Seismicity Predicted From 3-D Thermal Evolution Models of Interior Dynamics, *Geophys.*
359 *Res. Lett.* **45.6** 2580–2589.
- 360 Rivoldini, A., T. Van Hoolst, O. Verhoeven, A. Mocquet, and V. Dehant (2011). Geodesy constraints on the interior
361 structure and composition of Mars, *Icarus* **213.2** 451–472.
- 362 Ross, Z. E. and Y. Ben-Zion (2014). Automatic picking of direct P, S seismic phases and fault zone head waves, *Geophys.*
363 *J. Int.* **199.1** 368–381.
- 364 Schimmel, M. (1999). Phase cross-correlations: Design, comparisons, and applications, *Bull. Seismol. Soc. Am.* **89.5** 1366–
365 1378.
- 366 Schimmel, M., E. Stutzmann, F. Ardhuin, and J. Gallart (2011a). Polarized Earth’s ambient microseismic noise, *Geochem.*
367 *Geophys. Geosys.* **12.7**.
- 368 Schimmel, M., E. Stutzmann, and J. Gallart (2011b). Using instantaneous phase coherence for signal extraction from
369 ambient noise data at a local to a global scale, *Geophys. J. Int.* **184.1** 494–506.
- 370 Selby, N. D. (2001). Association of Rayleigh Waves Using Backazimuth Measurements : Application to Test Ban Verifica-
371 tion, *Bull. Seismol. Soc. Am.* **1.3** 580–593.
- 372 Spiga, A., D. Banfield, N. A. Teanby, F. Forget, A. Lucas, B. Kenda, J. A. Rodriguez Manfredi, R. Widmer-Schmidrig,
373 N. Murdoch, M. T. Lemmon, R. F. Garcia, L. Martire, Ö. Karatekin, S. Le Maistre, B. Van Hove, V. Dehant, P.
374 Lognonné, N. Mueller, R. Lorenz, D. Mimoun, S. Rodriguez, É. Beucler, I. Daubar, M. P. Golombek, T. Bertrand,
375 Y. Nishikawa, E. Millour, L. Rolland, Q. Brissaud, T. Kawamura, A. Mocquet, R. Martin, J. Clinton, É. Stutzmann,
376 T. Spohn, S. Smrekar, and W. B. Banerdt (2018). Atmospheric Science with InSight, *Space Sci. Rev.* **214.7**.
- 377 Spohn, T., M. Grott, S. E. Smrekar, J. Knollenberg, T. L. Hudson, C. Krause, N. Müller, J. Jänchen, A. Börner, T.
378 Wippermann, O. Krömer, R. Lichtenheldt, L. Wisniewski, J. Grygorczuk, M. Fittock, S. Rheershemius, T. Sprowitz,

379 E. Kopp, I. Walter, A. C. Plesa, D. Breuer, P. Morgan, and W. B. Banerdt (2018). The Heat Flow and Physical
380 Properties Package (HP3) for the InSight Mission, *Space Sci. Rev.* **214.5**.

381 Stähler, S. C. and K. Sigloch (2014). Fully probabilistic seismic source inversion – Part 1: Efficient parame-
382 terisation, *Solid Earth* **5.2** 1055–1069.

383 Teanby, N. (2015). Predicted detection rates of regional-scale meteorite impacts on Mars with the InSight short-period
384 seismometer, *Icarus* **256** 49–62.

385 Van Driel, M., L. Krischer, S. C. Stähler, K. Hosseini, and T. Nissen-Meyer (2015). Instaseis: instant global seismograms
386 based on a broadband waveform database, *Solid Earth* **6.2** 701–717.

387 Vidale, J. E. (1986). Complex polarization analysis of particle motion, *Bull. Seismol. Soc. Am.* **76.5** 1393–1405.

388 Wieczorek, M. A. and M. Zuber (2004). Thickness of the Martian crust: Improved constraints from geoid-to-topography
389 ratios, *J. Geophys. Res.* **109.E1** E01009.

390 Zharkov, V. N. and T. V. Gudkova (2005). Construction of Martian interior model, *Sol. Syst. Res.* **39.5** 343–373.

391 Zheng, Y. and H. Hu (2017). Nonlinear Signal Comparison and High-Resolution Measurement of Surface-Wave Dispersion,
392 *Bull. Seismol. Soc. Am.* **107.3** 1551–1556.

393 Zheng, Y., F. Nimmo, and T. Lay (2015). Seismological implications of a lithospheric low seismic velocity zone in Mars,
394 *Phys. Earth Planet. Inter.* **240** 132–141.

395 List of Figures

396	1	Catalogue summary maps: distribution of impacts (left) and marsquakes (right) in the true catalogue, both 397 randomly distributed over the sphere. The maps are centered on the InSight landing site (white triangle). 398 Only a fraction of these events were detectable above the noise level. 20	
399	2	Statistics for marsquakes in the true catalogue: (left) The magnitude-frequency distribution approximates 400 a Gutenberg-Richter distribution with b-value 1.0. The largest event in the catalogue has a magnitude 401 $M_w = 5.0$. (right) The magnitude-depth distribution of the marsquakes in the true catalogue is a skewed 402 Gaussian with a maximum event number around 20 km and maximum allowed event depth of 80 km. . . . 21	
403	3	Summary of the model EH45TcoldCrust1b that was used in the blind test. Vertical profile of (A) seismic 404 velocities and density, (B) dispersion curves, and (C) travel times. This model includes a low-velocity zone 405 (LVZ, a region with a negative velocity gradient for either or both P and S). The LVZ leads to broad shadow 406 zones for direct-arriving S-phases as indicated by gaps in the travel time curves in (C). 22	
407	4	The most visible events in the data set, plotted as a function of distance from the station. Travel time curves 408 for the most prominent phases are shown in the legend. The waveforms are bandpass filtered between 1.5 409 and 10 s. 23	

410	5	Summary of the team performances: total number of detected events in the submitted catalogues (blue);	
411		detected events that can be associated with an event in the true catalogue (orange); detected events in the	
412		submitted catalogues with full locations provided (green); and number of these events that lie within L1	
413		mission requirements (red). Note the difference between orange and blue indicates false detections.	24
414	6	Temporal overview of the submitted catalogues indicating correct detections and locations as well as double	
415		and false detections. All events in the true catalogue are shown, red and green correspond to correct	
416		detection and correct location, those in gray are missing in the submitted catalogue. Marsquakes are shown	
417		as circles, and impacts as stars. Note the scale based on linear momentum p for the impacts on the right	
418		hand side.	25
419	7	Distance-magnitude summary for the six most complete submitted catalogues. All events in the true	
420		catalogue are shown for each team, correctly detected in red, correctly located in green and missed events	
421		in gray. The dashed lines approximate the detection threshold (gray dashed line) and correct location	
422		threshold (black dashed line) for MQS. Histograms at the top and right side show the number of correctly	
423		detected (red), correctly located (green) and missed events (gray) for a number of distance and magnitude	
424		bins.	26
425	8	Distance performance - comparing the distances provided in the six most complete submitted catalogues	
426		with the true event distance. Gray area marks the L1 requirement. Note that for an event to be located	
427		within L1 we also required correct azimuth and origin time. For MQS, their data quality classification is	
428		indicated.	27
429	9	Back-azimuth performance for the six most complete submitted catalogues in terms of the back-aimuth	
430		estimation error as a function of distance. The gray area marks the mission L1 requirement. Note that for	
431		an event to be located within L1 we also required correct distance and origin time.	28
432	10	Origin time performance for the five most complete submitted catalogues in terms of the timing error as	
433		a function of distance. Note that there is no L1 requirement, but for an event to be located within L1 we	
434		required correct azimuth and distance. Oxford's catalogue did not include origin times, but only arrival	
435		times; hence it is omitted here.	29

436 11 (top) Location and vertical component waveforms for the three strongest impact signals in the true cat-
 437 alogue. On the map, the impacts are indicated by stars (size proportional to the linear momentum), the
 438 station is marked with the triangle. The closest event was correctly identified as an impact by MQS. Though
 439 some other teams identified the largest event, no other team classified it as an impact in their catalogues.
 440 (bottom) Similar plot for three quakes for comparison. Seismic phases in both plots are annotated as:
 441 S1/P1 - first arriving S/P wave, where S was only visible on the tranverse component, G1/R1 - minor arc
 442 Love/Rayleigh waves, OT - source origin time. 30

Table 1: Contributions to the blind test data set
responsible co-authors (alphabetically ordered by last names)

contribution	
marsquake catalogue	Savas Ceylan, John Clinton, Martin van Driel
impact catalogue	Ingrid Daubar, Matthew P. Golombek
synthetic seismograms	Martin van Driel, Melanie Drilleau
synthetic noise and pressure	Melanie Drilleau, Raphael Garcia, Balthasar Kenda, Philippe Lognonné, David Mimoun, Naomi Murdoch, Ludovic Perrin, Aymeric Spiga
compilation of 1D models	Amir Khan, Mark P. Panning
compilation of the data set and webservices	Savas Ceylan, Martin van Driel, Fabian Euchner
final choice of 1D model and catalogues	Bruce Banerdt, Martin van Driel
test conception and initiation	Domenico Giardini, Philippe Lognonné

Table 2: Participating teams and their members

group name	team members (alphabetically ordered by last names)
Bochum	Marc S. Boxberg, Manuel Ditz, Andre Lamert, Thomas Möller, Marcel Paffrath
Colorado	Shane Zhang
Geoazur	Hector Alemany, David Ambrois, Julien Balestra, Jérôme Chèze, Anne Deschamps, Diego Mercerat, Fabrice Peix, Lucie Rolland, Cédric Twardzik
SEISonMars@school	French Seismological Educational Network (SISMOS à l'Ecole) coordinated by Julien Balestra
Hamburg	Dirk Becker, Titus Casademont, Fabian Dethof, David Essing, Katharina Grunert, Celine Hadzioannou, Isabell Hochfeld, Tabea Kilchling, Sarah Mader, Lorenz Marten, Franziska Mehrkens, Paul Neumann, Robert Neurath, Christoph Schröer, René Steinmann, Noah Trumpik, Philipp Werdenbach-Jarklowski
Houston	Hao Hu, Jiaxuan Li, Yingcai Zheng
IPGP	Martin Schimmel, Eleonore Stutzmann
Max Planck	Conny Hammer, Brigitte Knapmeyer-Endrun
MQS	Maren Böse, Nienke Brinkman, Savas Ceylan, John Francis Clinton, Fabian Euchner, Domenico Giardini, Sharon Kedar, Amir Khan, Simon Christian Stähler
Oxford	Benjamin Fernando, Thomas Garth, Harriet Godwin, Claudia Haindl, Kasra Hosseini, Alexandre Szenicer, Maria Tsekhmistrenko
Utah	Amir Allam

Table 3: Overview of participating teams and methods employed

group name	methods
Bochum	detection: STA/LTA triggering and manual review; location: three probabilistic polarization analysis methods for azimuth (Eisermann et al. 2015; Selby 2001); probabilistic body wave and Rayleigh group traveltimes for distance (Panning et al. 2015; Böse et al. 2016).
Colorado	detection: manual event detection on bandpass filtered traces; location: probabilistic polarization analysis for azimuth (Böse et al. 2016); probabilistic body wave and Rayleigh group traveltimes for distance (Panning et al. 2015); magnitudes: Clinton et al. 2017; other efforts: attempt of pressure decorrelation (Murdoch et al. 2017a); verification of the methods on synthetics (van Driel et al. 2015; Ceylan et al. 2017).
Geoazur	detection: automated event detection using different STA/LTA triggers, manual classification; location: distance based on relative P-S traveltime, azimuth based on P and Rayleigh polarization (Jurkevics 1988; Bayer et al. 2012; Panning et al. 2015; Khan et al. 2016); other efforts: correct model chosen based on surface wave dispersion.
SEISonMars@school	detection: visual inspection of the data, manual event detection.
Hamburg	detection: visual (data and spectrograms) and automated event detection (STA/LTA triggers with variable parameter settings, spectrogram detector); location: visual azimuth determination using hodograms; distance based on relative P, S, R1 and multiple orbit surface waves; other efforts: correct model chosen based on traveltimes and dispersion curves; automated pressure event classification.
Houston	location: surface wave polarization for azimuth (Vidale 1986); relative surface wave traveltimes for distance (including minor arc only); other efforts: high resolution dispersion analysis of multi-orbit surface waves to determine phase velocity and the correct model (Zheng et al. 2015; Zheng and Hu 2017); depth based on depth phases.
IPGP	key efforts: autocorrelation to detect crustal discontinuities (Schimmel 1999; Schimmel et al. 2011b); degree of polarization Rayleigh wave detection and azimuth (Schimmel et al. 2011a); no catalogue submitted.
Max Planck	key efforts: automated event detection and classification using Hidden Markov Models (Hammer et al. 2012; Hammer et al. 2013; Knappmeyer-Endrun and Hammer 2015); no catalogue submitted.
Marsquake Service	detection: event detection by visual screening of spectrograms; location: four probabilistic methods for distance and azimuth for body and surface waves (Böse et al. 2016); new model set for probabilistic methods based on the largest events; distances refined by visual alignment of waveforms vs. distance for all events; multiple iterations in relocation to detect outliers; magnitudes: Böse et al. 2018; other efforts: event classification based on quality of location (Clinton et al. 2018); correct model chosen; by comparing event waveforms at similar distances, depths were indicated and one event was correctly identified as an impact.
Oxford	detection: visual event detection on bandpass filtered traces; location: differential traveltimes and surface wave dispersion for distance; particle motion and polarization for azimuth (three different methods); detailed description in Fernando et al. (2018); other efforts: three models suggested, including the correct one.
Utah	detection: manual event detection assisted by STA/LTA using multiple filter bands and polarization (Jurkevics 1988; Allam et al. 2014; Ross and Ben-Zion 2014); location: azimuth based on P and Rayleigh polarization; distance based on relative P and S traveltimes; other efforts: model wrongly detected based on H/V ratio (Lin et al. 2014) and receiver functions (Allam et al. 2017); event classification based on radial/transverse amplitude ratio.

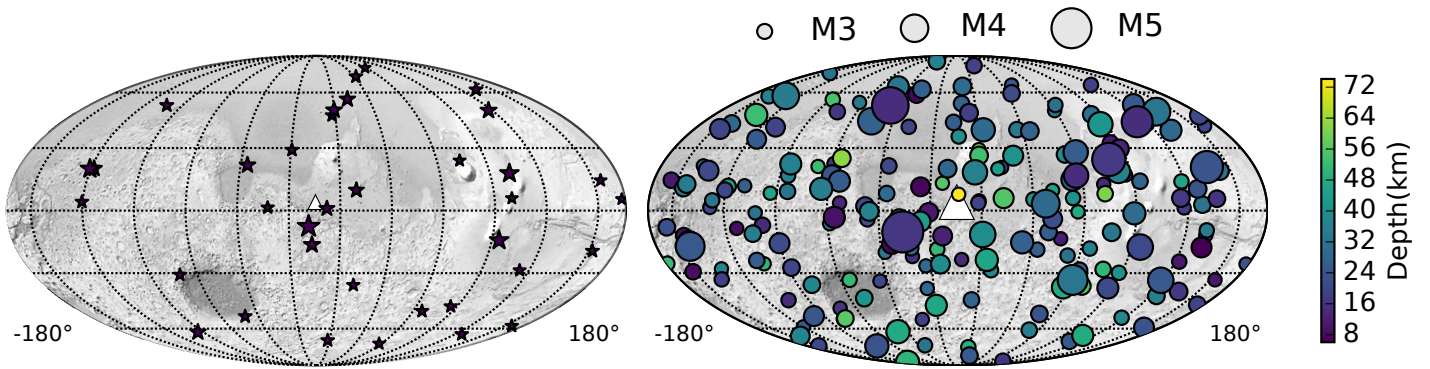


Figure 1: Catalogue summary maps: distribution of impacts (left) and marsquakes (right) in the true catalogue, both randomly distributed over the sphere. The maps are centered on the InSight landing site (white triangle). Only a fraction of these events were detectable above the noise level.

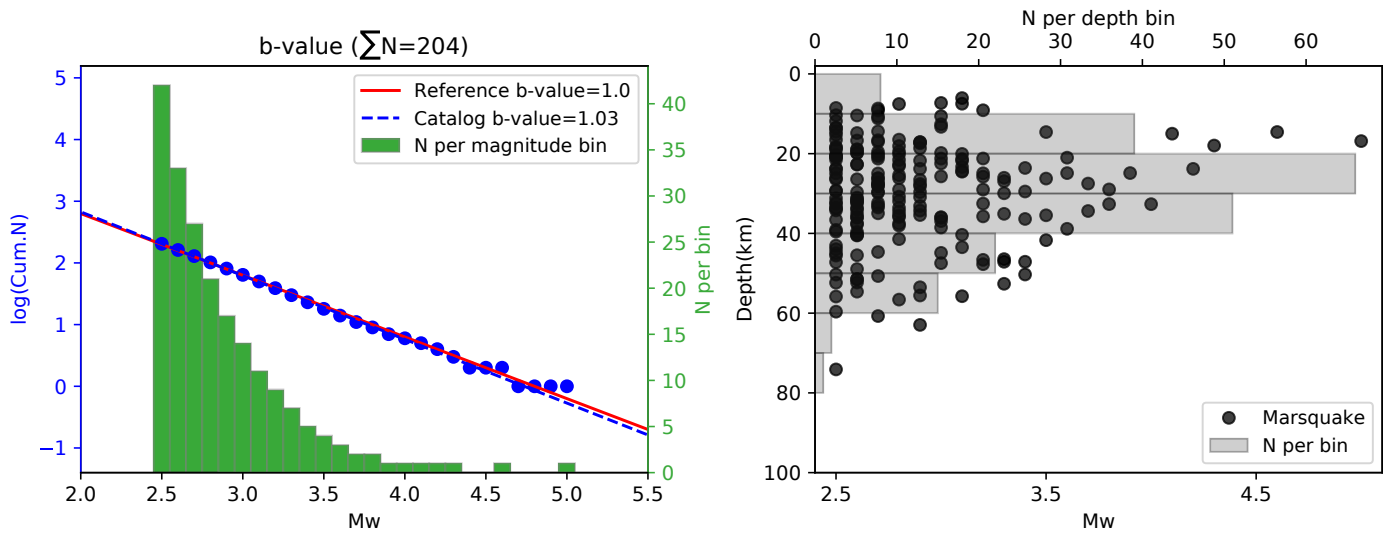


Figure 2: Statistics for marsquakes in the true catalogue: (left) The magnitude-frequency distribution approximates a Gutenberg-Richter distribution with b-value 1.0. The largest event in the catalogue has a magnitude $M_w = 5.0$. (right) The magnitude-depth distribution of the marsquakes in the true catalogue is a skewed Gaussian with a maximum event number around 20 km and maximum allowed event depth of 80 km.

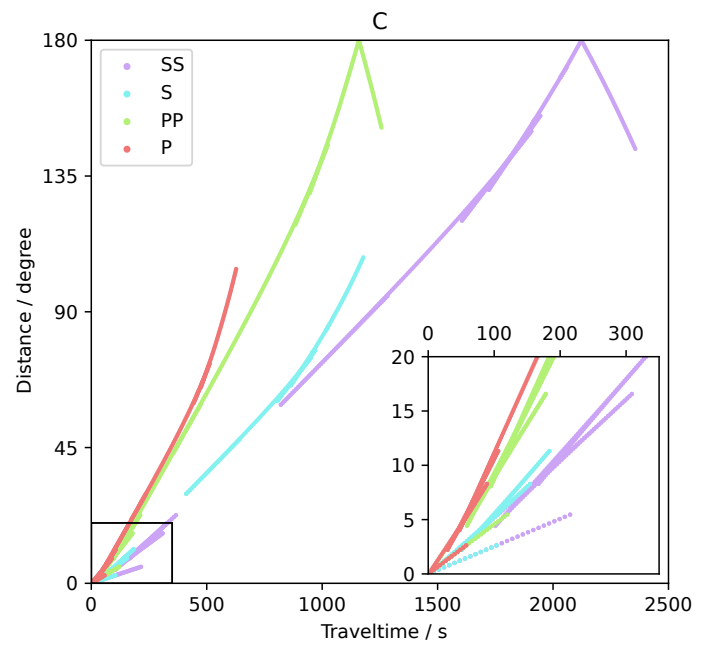
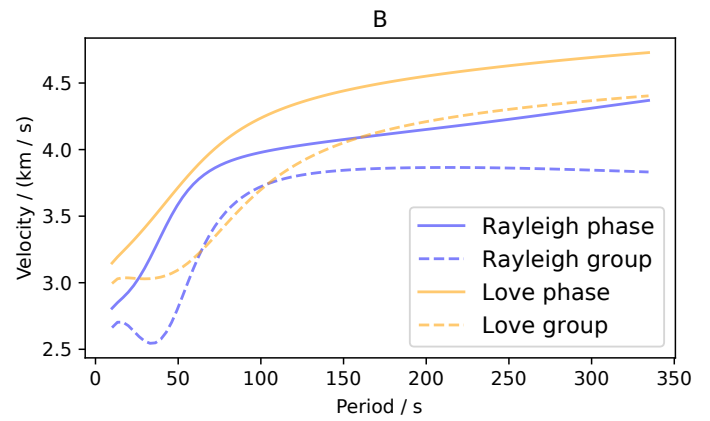
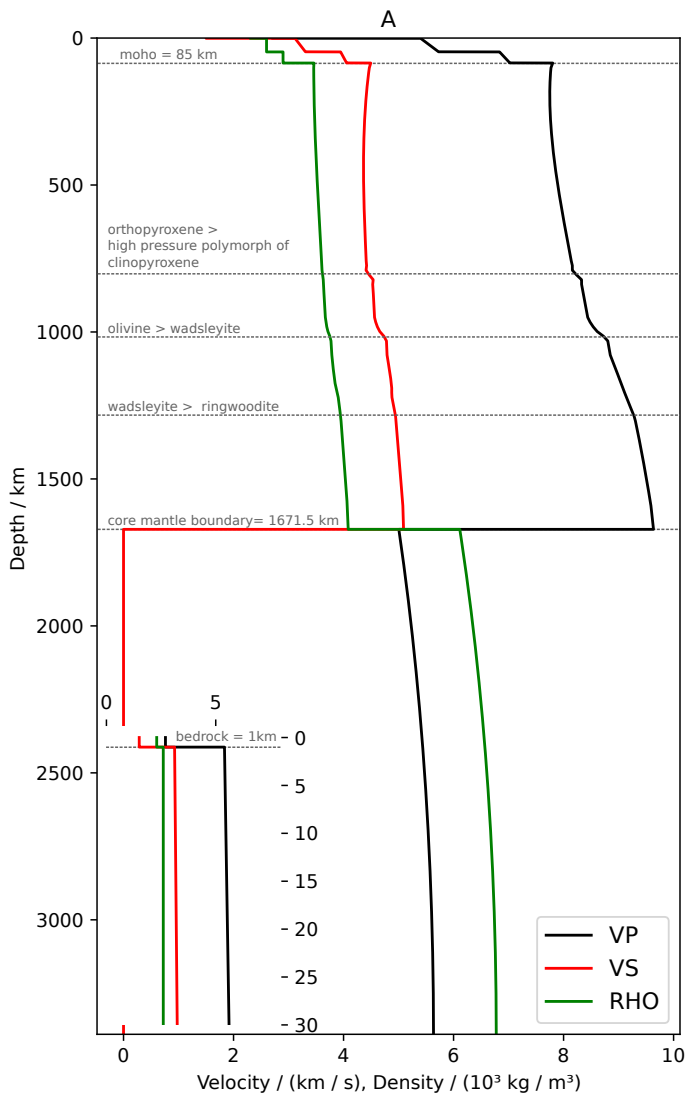


Figure 3: Summary of the model EH45TcoldCrust1b that was used in the blind test. Vertical profile of (A) seismic velocities and density, (B) dispersion curves, and (C) travel times. This model includes a low-velocity zone (LVZ, a region with a negative velocity gradient for either or both P and S). The LVZ leads to broad shadow zones for direct-arriving S-phases as indicated by gaps in the travel time curves in (C).

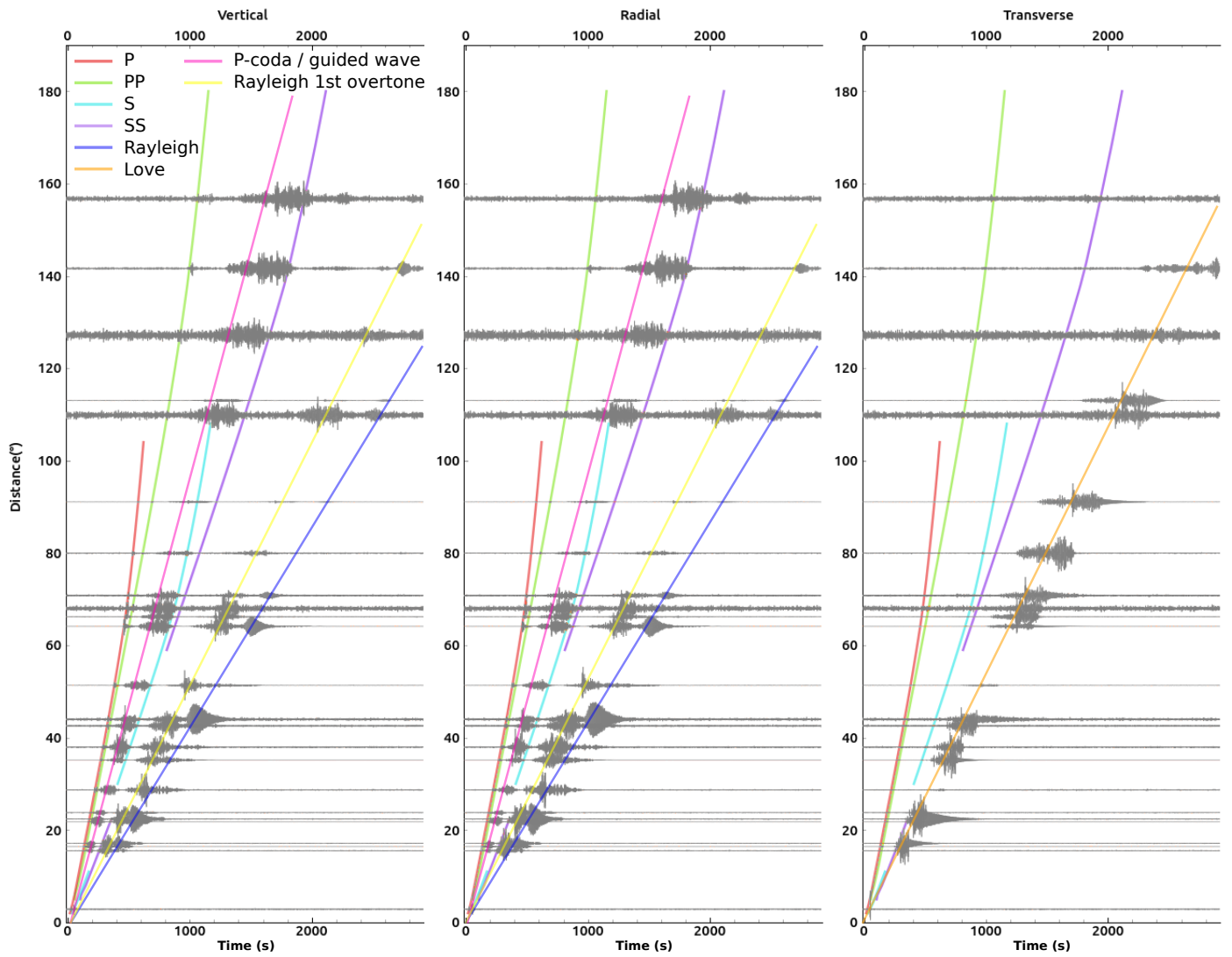


Figure 4: The most visible events in the data set, plotted as a function of distance from the station. Travel time curves for the most prominent phases are shown in the legend. The waveforms are bandpass filtered between 1.5 and 10 s.

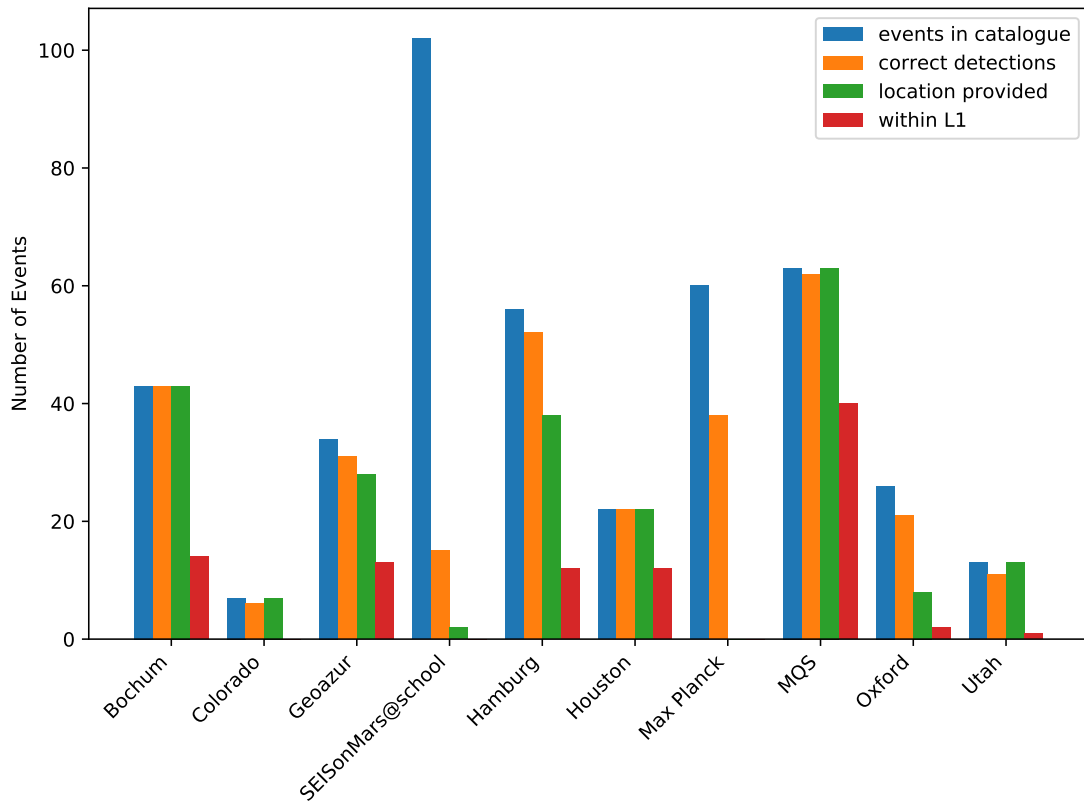


Figure 5: Summary of the team performances: total number of detected events in the submitted catalogues (blue); detected events that can be associated with an event in the true catalogue (orange); detected events in the submitted catalogues with full locations provided (green); and number of these events that lie within L1 mission requirements (red). Note the difference between orange and blue indicates false detections.

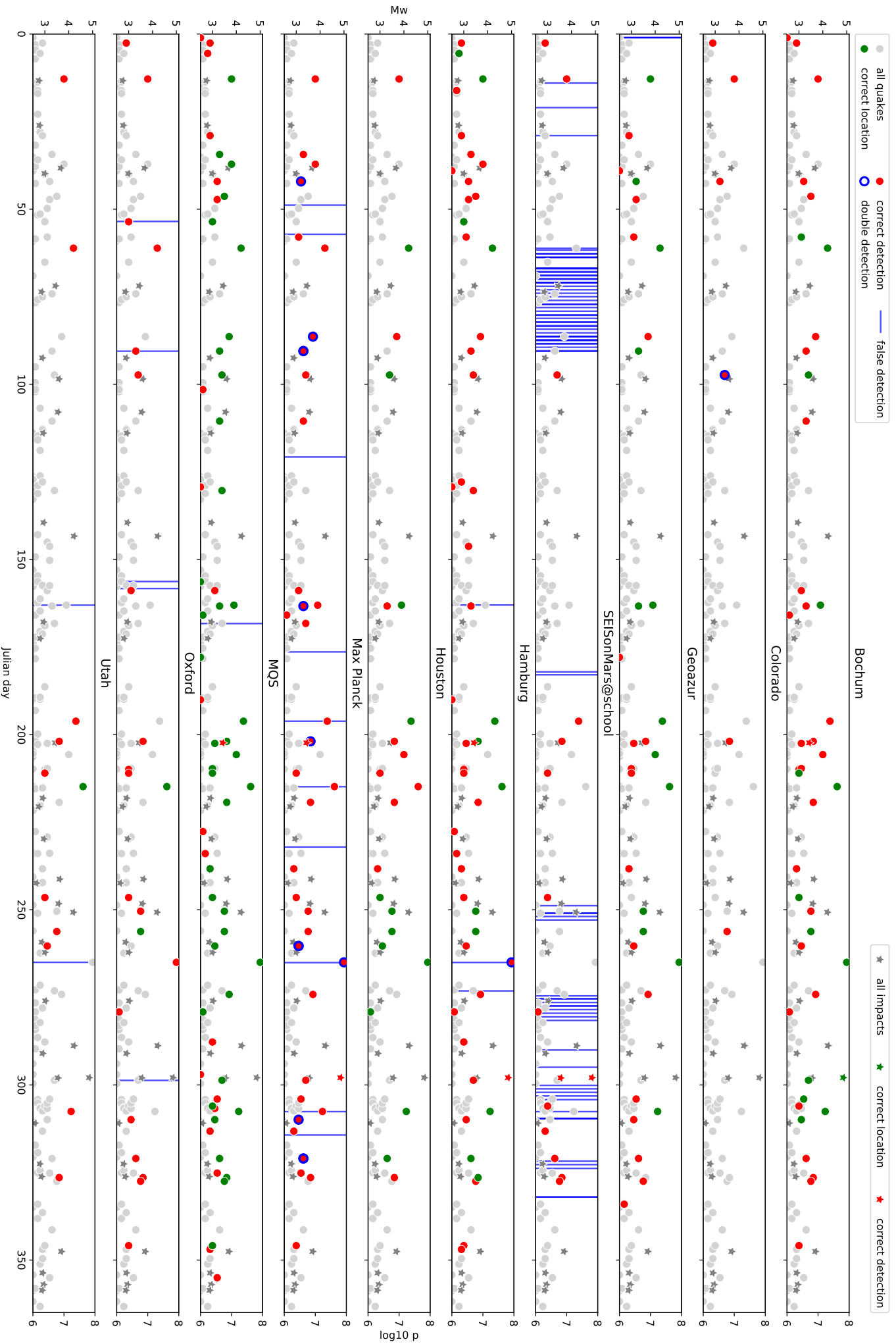


Figure 6: Temporal overview of the submitted catalogues indicating correct detections and locations as well as double and false detections. All events in the true catalogue are shown, red and green correspond to correct detection and correct location, those in gray are missing in the submitted catalogue. Marsquakes are shown as circles, and impacts as stars. Note the scale based on linear momentum p for the impacts on the right hand side.

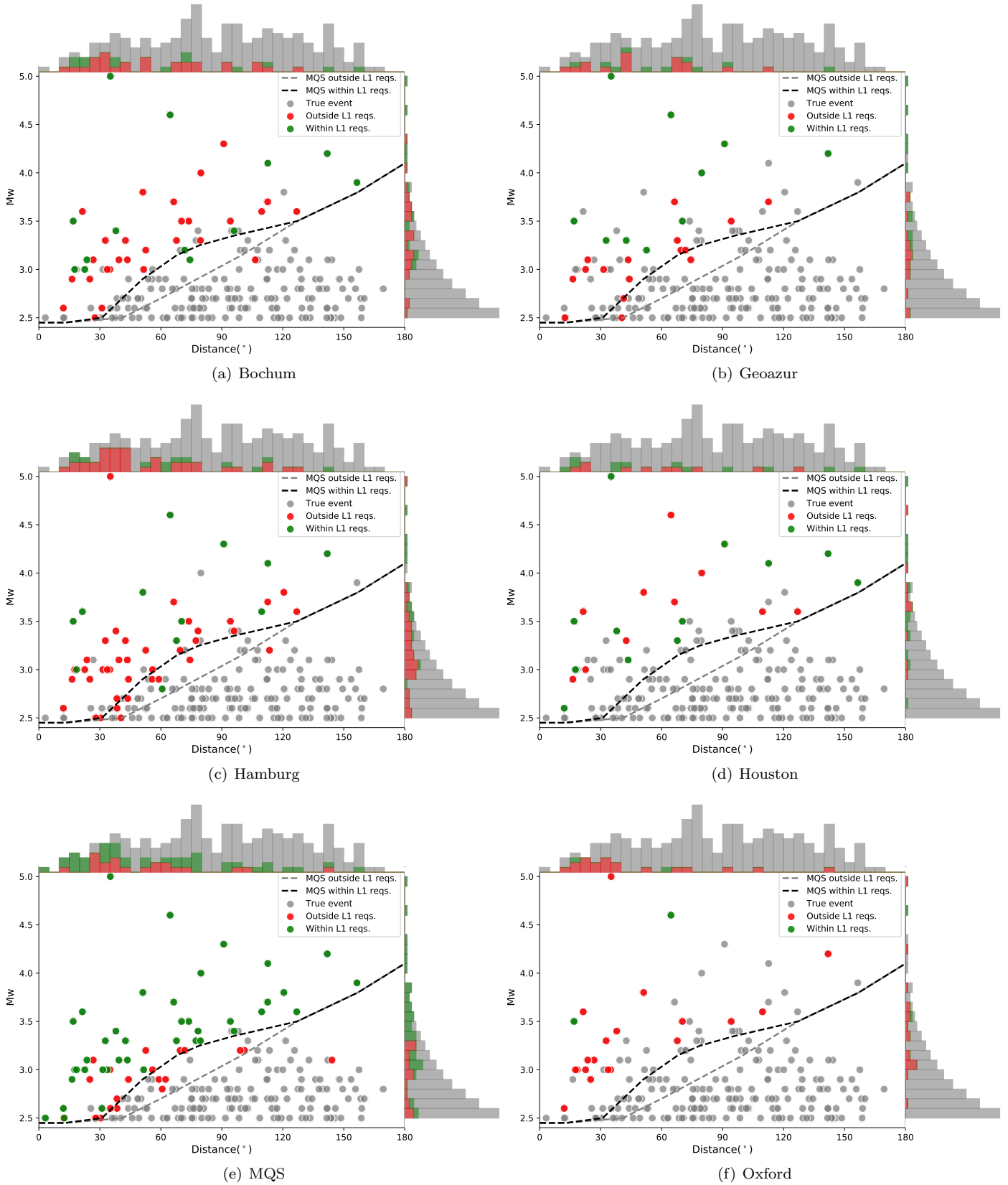


Figure 7: Distance-magnitude summary for the six most complete submitted catalogues. All events in the true catalogue are shown for each team, correctly detected in red, correctly located in green and missed events in gray. The dashed lines approximate the detection threshold (gray dashed line) and correct location threshold (black dashed line) for MQS. Histograms at the top and right side show the number of correctly detected (red), correctly located (green) and missed events (gray) for a number of distance and magnitude bins.

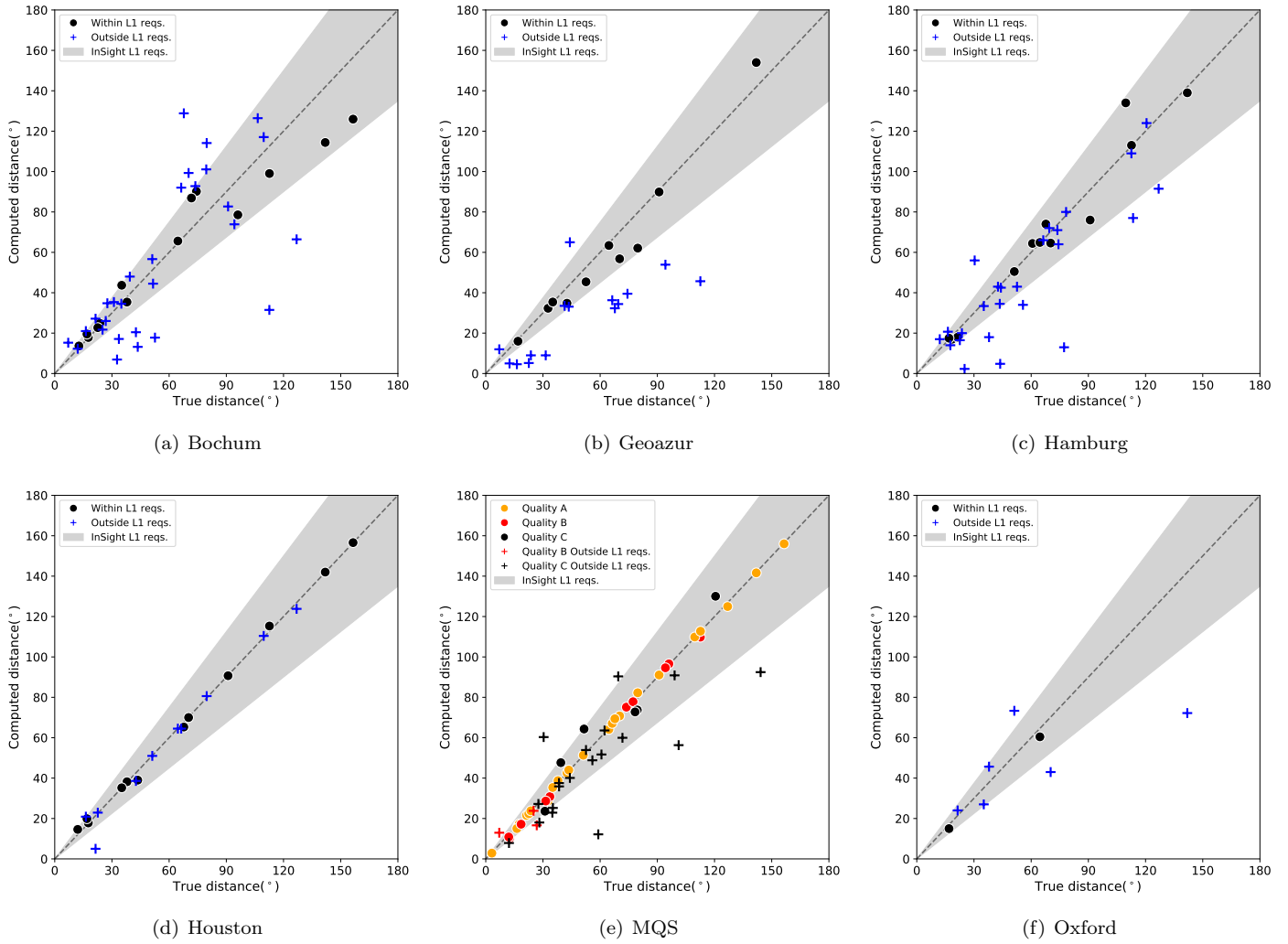


Figure 8: Distance performance - comparing the distances provided in the six most complete submitted catalogues with the true event distance. Gray area marks the L1 requirement. Note that for an event to be located within L1 we also required correct azimuth and origin time. For MQS, their data quality classification is indicated.

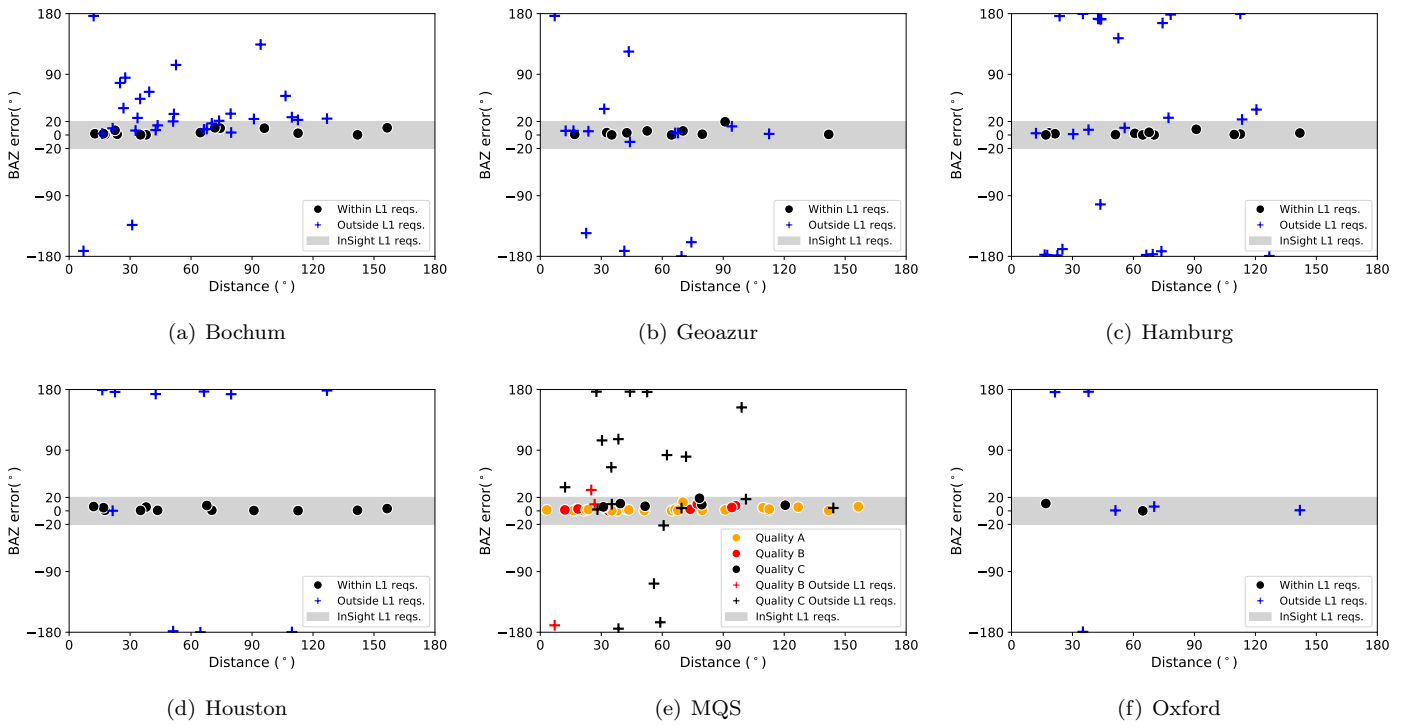


Figure 9: Back-azimuth performance for the six most complete submitted catalogues in terms of the back-azimuth estimation error as a function of distance. The gray area marks the mission L1 requirement. Note that for an event to be located within L1 we also required correct distance and origin time.

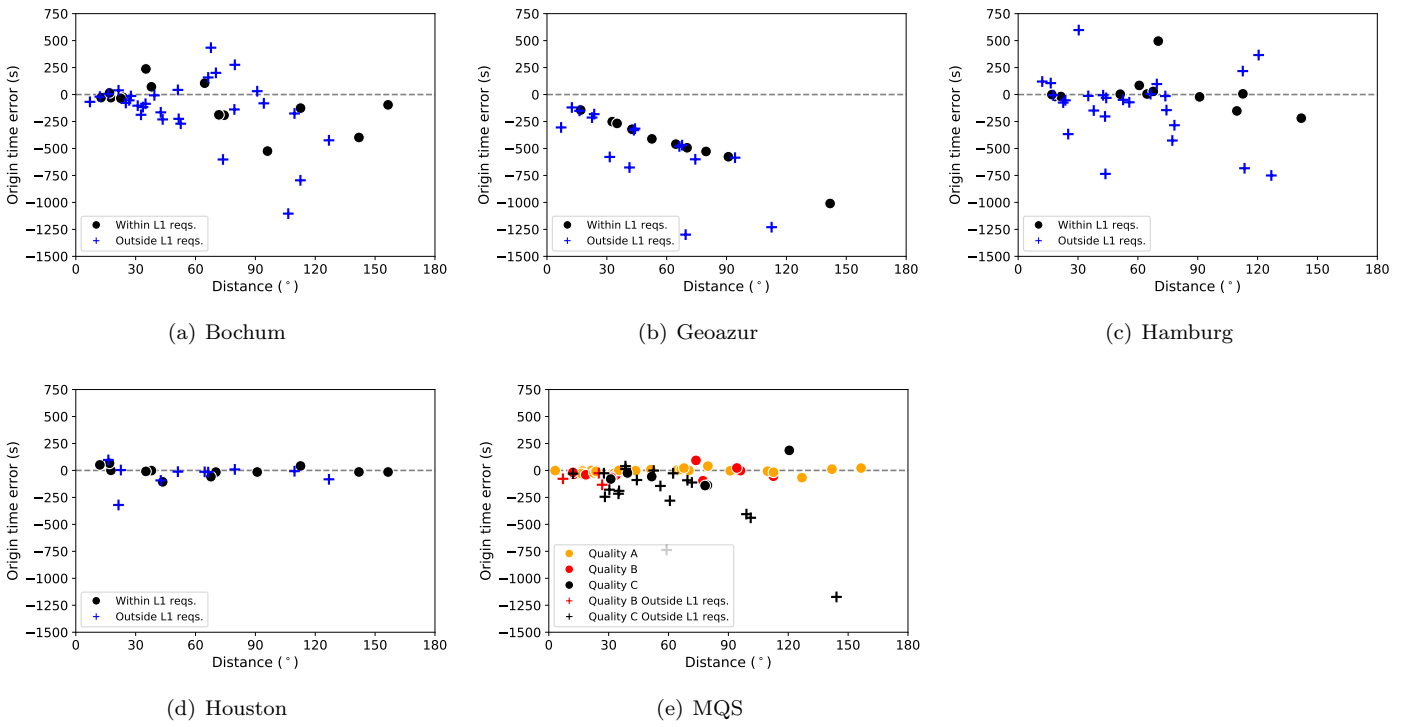


Figure 10: Origin time performance for the five most complete submitted catalogues in terms of the timing error as a function of distance. Note that there is no L1 requirement, but for an event to be located within L1 we required correct azimuth and distance. Oxford's catalogue did not include origin times, but only arrival times; hence it is omitted here.

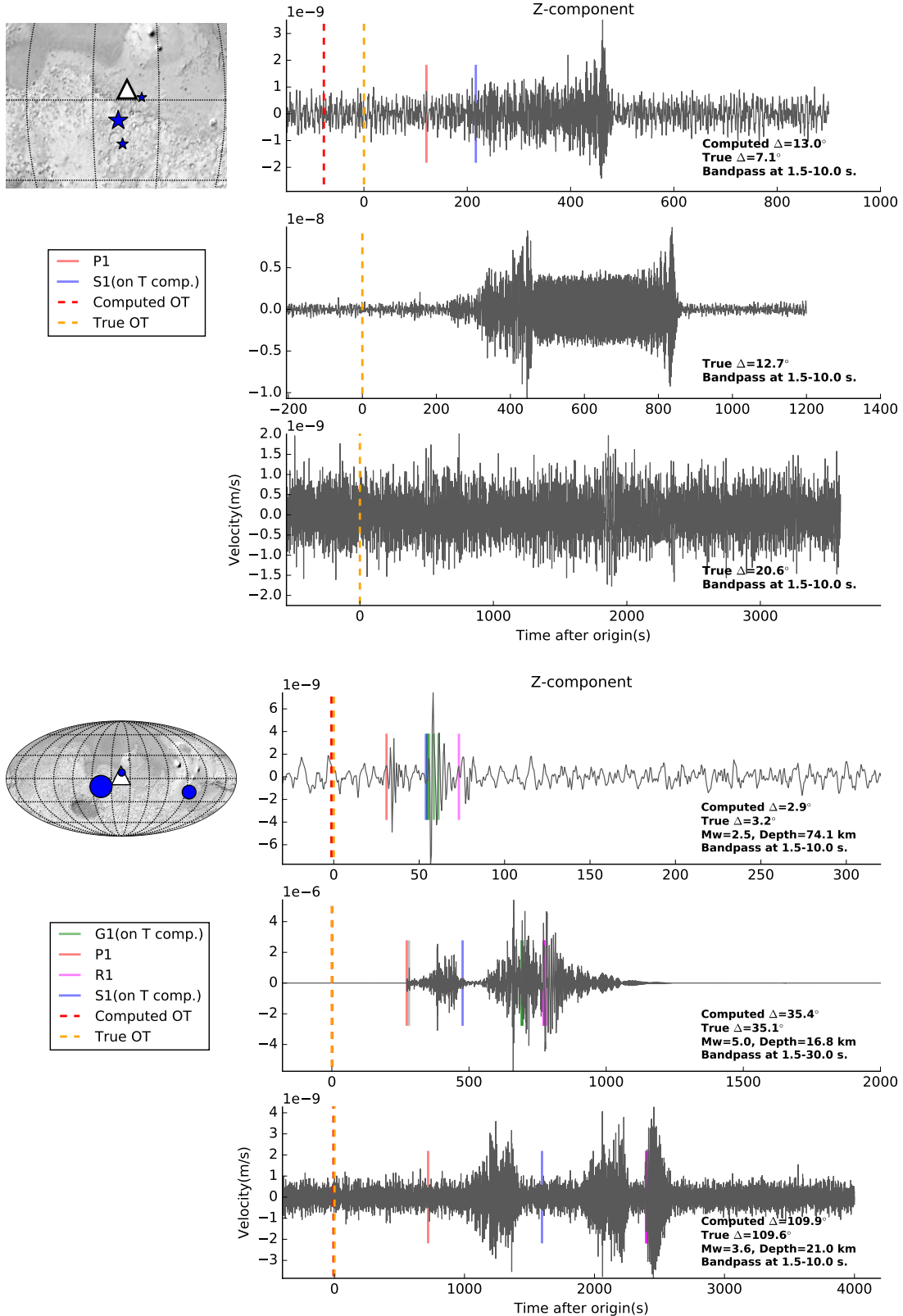


Figure 11: (top) Location and vertical component waveforms for the three strongest impact signals in the true catalogue. On the map, the impacts are indicated by stars (size proportional to the linear momentum), the station is marked with the triangle. The closest event was correctly identified as an impact by MQS. Though some other teams identified the largest event, no other team classified it as an impact in their catalogues. (bottom) Similar plot for three quakes for comparison. Seismic phases in both plots are annotated as: S1/P1 - first arriving S/P wave, where S was only visible on the transverse component, G1/R1 - minor arc Love/Rayleigh waves, OT - source origin time.